ACS APPLIED MATERIALS & INTERFACES

Research Article

www.acsami.org

Core–Shell Nanophosphor Architecture: Toward Efficient Energy Transport in Inorganic/Organic Hybrid Solar Cells

Qinghua Li,*[,†] Yongbiao Yuan,[†] Zihan Chen,[†] Xiao Jin,[†] Tai-huei Wei,[‡] Yue Li,[†] Yuancheng Qin,[†] and Weifu Sun*[,§]

[†]Key Laboratory of Jiangxi Province for Persistant Pollutants Control and Resources Recycle, Nanchang Hangkong University, Nanchang, 330063, P. R. China

[‡]Department of Physics, National Chung-Cheng University, Chia-Yi 621, Taiwan, Republic of China

[§]School of Materials Science and Engineering, The University of New South Wales, Sydney, NSW 2052, Australia

Supporting Information

ABSTRACT: In this work, a core–shell nanostructure of samarium phosphates encapsulated into a Eu^{3+}-doped silica shell has been successfully fabricated, which has been confirmed by X-ray diffraction, transmission electron microscopy (TEM), and high-resolution TEM. Moreover, we report the energy transfer process from the Sm^{3+} to emitters Eu^{3+} that widens the light absorption range of the hybrid solar cells (HSCs) and the strong enhancement of the electron-transport of TiO_2/poly(3-hexylthiophene) (P3HT) bulk heterojunction (BHJ) HSCs by introducing the unique core–shell nanoarchitecture. Furthermore, by applying femtosecond transient absorption spectroscopy, we successfully obtain the electron transport lifetimes of BHJ systems with or without incorporating the core–shell nanophosphors (NPs). Concrete evidence has been provided that the doping of core–shell NPs improves the efficiency of electron transfers from donor to acceptor, but the hole transport almost remains unchanged. In particular, the hot electron transfer lifetime was shortened from 30.2 to 16.7 ps, i.e., more than 44% faster than pure TiO_2 acceptor. Consequently, a notable power conversion efficiency of 3.30% for $SmPO_4$@Eu^{3+}:SiO_2 blended TiO_2/P3HT HSCs is achieved at 5 wt % as compared to 1.98% of pure TiO_2/P3HT HSCs. This work indicates that the core–shell NPs can efficiently broaden the absorption region, facilitate electron-transport of BHJ, and enhance photovoltaic performance of inorganic/organic HSCs.

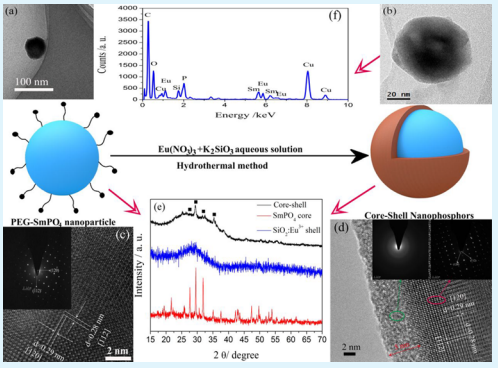

KEYWORDS: *inorganic/organic hybrid solar cell, core–shell nanophosphor, charge photogeneration dynamics, bulk heterojunction, energy transfer*

1. INTRODUCTION

Inorganic/organic hybrid solar cells (HSCs), electrochemical devices converting solar energy to electricity and having the characteristics of high power conversion efficiency (PCE), low fabrication cost, and being an environmental-friendly source of renewable energy, have attracted increasing interest as an alternative and promising solution for fossil energy depletion, environmental pollution, and ecological destruction.[1−3] Such inorganic/organic HSCs can take advantage of the beneficial properties of both types of materials such as low-cost solution processing of polymer semiconductors and high electron mobility of inorganic semiconductors.[4,5] Despite the advantages of inorganic/organic HSCs, as a relatively newly emerging or revived hotspot, it is still challenging to attain the desirable efficiency for these bulk heterojunction (BHJ) solar cells based on inorganic nanoparticles (e.g., TiO_2) and conducting polymers like poly(3-hexylthiophene) (P3HT). Over the last five years, most of the reported PCEs of solar cells based on P3HT are around 2%, ranging from 1.0−3.0%,[4,6−8] depending on the type of inorganic nanocrystals (except quantum dots, which are more related to colloidal quantum dot solar cells),[9] their morphology, and other factors.[10−12] In recent years, various methods have been developed to optimize the semiconductor, such as modifications utilizing nanotubes or nanoparticles.[13−16] However, efficiencies of the HSCs are still low at the current stage of development, which restricts its potential applications. One of the principal factors limiting high conversion efficiencies is its incapacity to utilize the near-infrared and infared photons of the solar spectrum. To overcome this limitation, one promising solution is to broaden the absorption range of the solar cells and utilize most of the solar ultraviolet and infrared irradiations by rare-earth ions doped down-conversion phosphors.[17−19] Especially, trivalent lanthanide (Ln^{3+}, in particular Sm^{3+} and Eu^{3+}) ions doped nanocrystals with various core–shell architecture composites can facilitate the energy transfer (ET) from sensitizer to

Received: May 6, 2014
Accepted: June 26, 2014
Published: June 26, 2014

activator and make for the successive photon absorption and energy transfer steps on account of their ladder-like energy levels.[20,21] Compared to the conventional luminescent materials such as organic fluorescent dyes, organic conducting polymer, and quantum dots (QDs), the Ln^{3+} ions doped core−shell composites have more superior features, such as narrow emission band widths (<10 nm), long luminescence lifetime, and low long-term toxicity. The core−shell architecture also effectively allows a facile modulation of activator composition and concentration while minimizing luminescence quenching.[22−24] With such benifits of Ln^{3+} ions doped core−shell NPs, we envision that core−shell NPs should also be critical to inorganic/organic HSCs since the solution-processed light-harvesting films prepared by techniques such as bath soaking are typically amorphous or poorly crystalline,[25] consequently suffering from poor charge-carrier transport. Nonetheless, to the best of our knowledge, there are few reports on the combination of down-conversion (DC) luminescence of Ln^{3+} doped NPs into a single nanosystem by core−shell engineering to simultaneously broaden solar absorption range and improve charge carrier transport. Furthermore, few significant attempts on the doping effect of rare-earth compounds has been made in the inorganic/organic HSCs thus far. And the innate dynamics of the photoexcited electrons and holes and the origin of driving the high efficiency of HSCs by introducing the core−shell NPs have not been explored yet, albeit the application of rare-earth compound dopant in solar cells have been demonstrated in the previous works.[26−28]

To validate our hypothesis, we conduct an experimental investigation of Ln^{3+} ions codoped core−shell NPs by taking advantage of the Sm^{3+} ions acting as the sensitizer and Eu^{3+} ions acting as the activator, and the merit of core−shell nanostructures. And a novel design by incorporating Sm^{3+} and Eu^{3+} codoped core−shell NPs into TiO_2 films in a bid to promote electron−hole transport at the interface of inorganic/organic BHJ will be reported. To elucidate the origin of the efficiency enhancement of HSCs, through pump−probe spectroscopy and femtosecond transient absorption spectroscopy, we successfully monitored the electron dynamic, hole dynamic, and electron−hole recombination. Concrete evidence has been provided that electron transport at the interface of the BHJ has been improved. A novel BHJ solar cell based on the core−shell NPs:TiO_2 acceptor was fabricated, and its photovoltaic characteristics were correspondingly probed.

2. EXPERIMENTAL SECTION

Materials. Chemical reagents including tetrabutyl titanate, polyethylene glycol (PEG, molecular weight of 20000), nitric acid, phosphoric acid, P25(Degussa), OP emulsifying agent (Triton X-100), europium nitrate, samarium nitrate, diammonium hydrogen phosphate, potassium silicate hydrate, acetonitrile, and isopropanol are analytic purity and were purchased from Aldrich, Hong Kong, China. P3HT and poly(3, 4-ethylenedioxylenethiophene)-polystylene sulfonic acid (PEDOT:PSS) were provided by Aldrich. Fluorine-doped tin oxide glass (FTO, sheet resistance 8 Ω cm^{-2}) was purchased from Hartford Glass Co., USA.

Synthesis of PEG-Modified $SmPO_4$ Core Flocculent Precursor Solution. Monodispersed PEG-modified $SmPO_4$ cores were prepared using a simple and effective sol−gel method.[29−31] Samarium nitrate (0.03 mmol) was put into the dilute nitric acid and heated and stirred simultaneously. After complete dissolution, the $(NH_4)_2HPO_4$ (0.05 mol) with PEG aqueous solution (8 mL, 0.2 mol mL^{-1}) was added by magnetic stirring for 30 min, and then, the solution changed into a white flocculent liquid. Subsequently, the mixture was heated to 60 °C, continuously stirred for 20 min, and then cooled to room temperature. Finally, the resultant PEG-modified $SmPO_4$ precursor solution was kept in an oven at 30 °C for further experiments.

Synthesis of $SmPO_4$@Eu^{3+}-Doped SiO_2 Core−Shell Nanophosphors. Core−shell nanophosphors were prepared by a minor modification of the hydrothermal method.[21,32−34] $Eu(NO_3)_3$ (0.025 mmol) was added to a mixture of distilled water (25 mL) and ethanol (25 mL). Then the as-prepared PEG-modified $SmPO_4$ core precursor solution (5 mL) was added to the mixture with the assistance of sonication for 30 min, followed by vigorous stirring for 20 min. The mixture was quickly transferred into a Teflon-lined stainless-steel autoclave, followed by adding K_2SiO_3 (0.100 mol) into the autoclave under stirring. Afterward, appropriate deionized water was added until the filled degree reached 80% of the total container volume. Then, the obtained solution was hydrothermally treated at 200 °C for 12 h. After being naturally cooled to room temperature, the obtained product was centrifuged and then dried in air at ambient temperature, followed by sintering in air at 850 °C for 30 min.

Preparation of Core−Shell NPs:TiO_2 Acceptor Colloid. The core−shell NPs blended TiO_2 was prepared according to the previous report.[35−37] Tetrabutyl titanate (10 mL) was added to distilled water (100 mL) under stirring, followed by a white precipitate immediately. The precipitate was filtered, washed with distilled water, and then transferred to a mixed solution (150 mL) containing nitric acid (1 mL) and acetic acid (10 mL) at 80 °C. Under vigorous stirring, a light blue TiO_2 precursor was formed, followed by ultrasonic stirring for 30 min. Finally, the mixture was hydrothermally treated in an autoclave at 200 °C for 24 h to form TiO_2 colloid. Subsequently, the P25 (0.075 g) and core−shell NPs (0.375 g, 5 wt %) were added in TiO_2 colloid by repeating crystallization at 200 °C for 12 h. At last, the resultant slurry was concentrated to 1/5 of its original volume by thermal evaporation, and PEG-20000 (0.5 g) and a few drops of the Triton X-100 emulsification reagent were added; an even and stable TiO_2 colloid was produced.

Fabrication of Inorganic/Organic HSCs. A layer of acceptor colloid with a thickness of 250 nm was prepared by coating the TiO_2 colloid on FTO glass by spin-coating, followed by sintering in air at 450 °C for 30 min. Then the acceptor film was soaked in a 0.15 mmol/mL conjugated polymer P3HT methylbenzene solution for 12 h to uptake P3HT. Next, PEDOT:PSS layer was spin-coated onto the bulk heterojunction. Finally, Pt electrode was deposited on the top of the PEDOT:PSS layer by thermal evaporation under vacuum. Note that the active area of our solar cell device is about 0.25 cm^2 in this work.

Characterization. The phases were identified by a Rigaku MiniFlex II X-ray diffractometer using Cu Kα radiation (λ = 0.154 nm) at a power of 30 kV and 40 mA. The XRD data were collected in a scan mode with a scanning speed of 5° min^{-1} in the range between 15° and 70°. The microstructure of the core−shell nanophosphors were analyzed by means of HRTEM and selected area electron diffraction (SAED), which were carried out by using a transmission electron microscope (JEM-2010, JEOL Ltd.) working at 200 kV. Samples for TEM and HRTEM were prepared by ultrasonically dispersing the samples in absolute ethanol, placing a small volume of this suspension on carbon-enhanced copper grids, and drying in air. The morphologies of the TiO_2-based acceptor layer and the cross section of bulk heterojunction and the morphology of acceptor layer were characterized by using a field emission scanning electron microscope (FESEM, Hitachi S4800); energy dispersive X-ray spectroscopy (EDS) data were recorded by using an FESEM equipped with an EDS detector (OXFORD 7021). The surface roughness parameters and height profile were measured by atomic force microscopy (AFM, Veeco Dimension 3100 V, US). All samples were fixed on the magnetic disk and then located on top of the scanner tube. The laser beam was focused on the preselected spot of the surface. The tapping mode was operated to take the micrographs; The cyclic voltammetry (CV) results were obtained using a BAS 100B instrument (BASi Inc., USA) at room temperature and a scan rate of 50 $mV{\cdot}s^{-1}$ with 0.1 M $TBAPF_6$ in acetonitrile as the supporting electrolyte, a platinized platinum (1.0 cm^2) as the counter electrodes, and Ag/Ag^+ electrode as the reference electrode; the values are

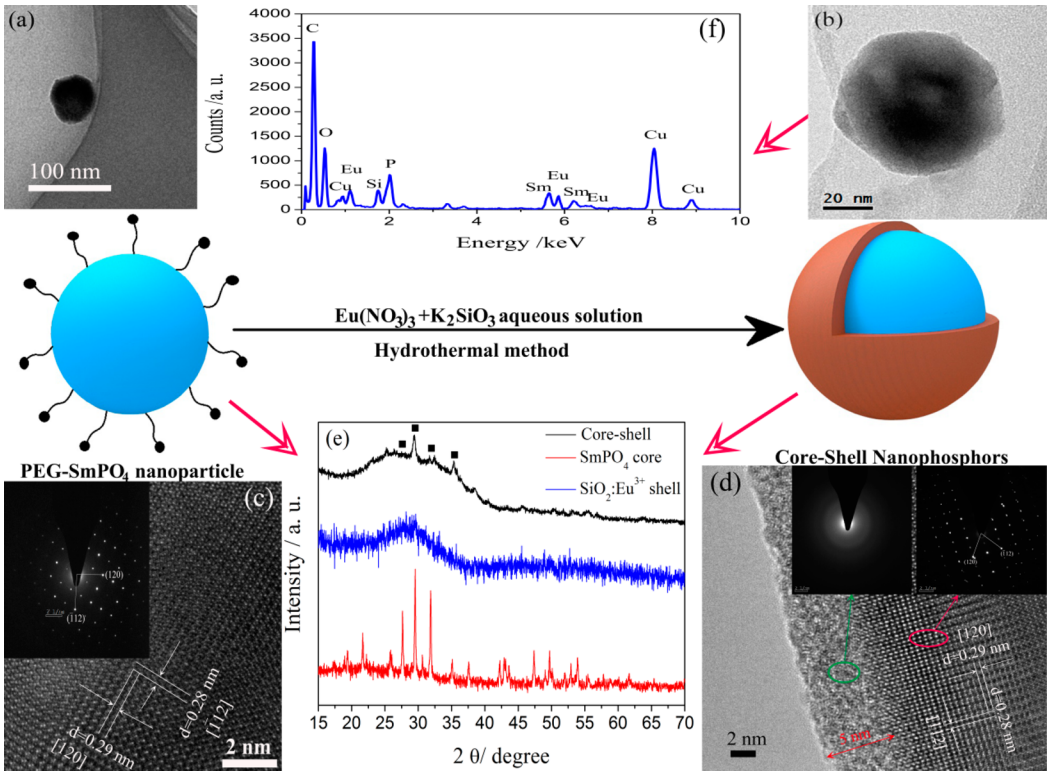

Figure 1. Schematic representation of the preparation of single crystalline $SmPO_4$@Eu^{3+}-doped silica core−shell NPs. TEM images of $SmPO_4$ nanoparticles (a) and core−shell nanophosphor (b), respectively. (c and d) HRTEM images of $SmPO_4$ nanoparticles and core−shell nanoposphor, respectively. (inset) SAED patterns of amorphous shell and crystalline core, respectively. (e) XRD patterns of Eu^{3+}-doped silica powder, $SmPO_4$ nanoparticles, and core−shell NPs, respectively. (f) EDS of core−shell nanophosphor.

expressed in potentials versus F_c/F_c^+. The pure TiO_2, core−shell nanophosphor films were used as work electrodes, respectively. Transient photoluminescence experiments were measured on a spectrometer (Bruker Optics 250IS/SM) with intensified charged coupled detector (Andor, IStar740). The samples were excited by 120 fs laser pulses at 400 nm with a repetition rate of 10 Hz. The time resolution was determined to be ∼60 ps; Charge photogeneration dynamics of the BHJs were measured by the mode-locked Ti:sapphire laser (Coherent Mira 900) in combination with a regenerative amplifier (Coherent Legend-F). The photoluminescence spectrum was measured by using a spectrophotometer (FLS920, Edinburgh), in which a xenon lamp and a photomultiplier tube (R955, Hamamatsu) were used as excitation source and fluorescence detector, respectively. The photocurrent−voltage (J−V) curves of the assembled HSCs were recorded on an Electrochemical Workstation (Xe Lamp Oriel Sol3A Class AAA Solar Simulators 94023A, USA) under irradiation of a simulated solar light from a 100 W xenon arc lamp in ambient atmosphere and the PCE was averaged based on at least 5 measurements. The incident photon-to-current conversion efficiency (IPCE) measurements were performed at short-circuit condition. A class A quality solar simulator (PEC-L11, AM1.5G, Peccell Technologies, Inc., Kanagawa, Japan) served as a light source. The light was directed through a monochromator (model 74100, Oriel Instrument, California, USA) onto the HSCs.

Time-resolved photoluminescence is measured on a spectrometer (Bruker Optics 250IS/SM) with intensified charge coupled device detector (Andor, IStar740). The ultrafast light source with a temporal resolution of ∼120 fs was generated by a mode-locked titanium-sapphire laser operating at 800 nm. An optical parametric amplifier (OPA-800CF-1, Spectra Physics) provided ultrashort laser pulses at desired wavelengths (∼120 fs, full width at half-maximum). A continuum white light generated from a sapphire plate was directed into the excited sample and detected by a charge coupled device (CCD) detector. Ultrashort laser pulses at 400 nm were employed as the pump light for the sample excitation and the probe light for the absorption measurement. Transient absorption at various delay times could be measured by controlling the arrival time of each laser pulse at the sample. The laser system was operated at a repetition rate of 10 Hz, thus each pulse excited fully relaxed sample. Each data was obtained by averaging 100 individual measurements to improve the signal-to-noise ratio, and the typical detection sensitivity of the difference absorption (ΔOD) was better than 10^{-4}.

3. RESULTS AND DISCUSSION

3.1. Characterization and Energy Transfer Process of Core−Shell NPs. In a typical procedure, polyethylene glycol (PEG) decorated $SmPO_4$ nanoparticles were first prepared and then used as seeds for growth of Eu^{3+}-doped silica shell as shown in Figure 1. The $SmPO_4$ nanoparticles and $SmPO_4$@Eu^{3+}-doped silica core−shell NPs were characterized by XRD, TEM, HRTEM, SAED, and EDS. Note that under almost identical experimental conditions, $SmPO_4$ nanoparticles, also denoted as A1, were achieved from PEG-modified $SmPO_4$ precursor solution by sintering in air at 850 °C for 30 min without the subsequent growth of Eu^{3+}-doped silica shell. The diameter of the obtained $SmPO_4$ nanoparticles was ∼50 nm (Figure 1a), whereas the diameter of core encapsulated in the core−shell NPs is about 40 nm only (Figure 1b). This is because the outer shell growth restricts the final size of the core (that is $SmPO_4$ nanoparticle) during the core−shell nanoarchitecture fabrication process. The formation of crystalline core−amorphous shell nanostructures was distinctly observed from the HRTEM image as shown in Figure 1d and further confirmed by the corresponding SAED patterns. In particular, the thickness of the Eu^{3+}-doped silica amorphous shell was about 4−6 nm, and this can be further confirmed by a sharp interface between the well-crystallized $SmPO_4$ core and

dx.doi.org/10.1021/am5027709 | ACS Appl. Mater. Interfaces 2014, 6, 12798−12807

amorphous silica shell (Supporting Information (SI), Figure S1d). In addition, the single crystalline core of core−shell NPs was further characterized (Figure 1c), which was markably single-crystalline structure without noticeable defects at atomic resolution. An estimated *d*-spacing of 0.29 and 0.28 nm was roughly evaluated from the lattice fringes, which well match with the lattice spacing of d_1 = 0.303 and d_2 = 0.281 nm corresponding to, respectively, (1,2,0) and ($\bar{1}$,1,2) planes of monoclinic-phase $SmPO_4$ (JCPDS card no.: 01-084-0918). Similarly, the values of *d*-spacing of 0.30 and 0.28 nm calculated from the SAED pattern as highlighted in the insets of Figure 1d are also in reasonable agreement with those obtained from XRD pattern of JCPDS 01-084-0918, i.e., d_1 = 0.303 and d_2 = 0.281 nm. All these results are indicative of single crystallinity of the core in the core−shell NPs and suggest that the composition of the core is mainly $SmPO_4$.

The XRD patterns of Eu^{3+}-doped silica shell, A1, and core−shell NPs with θ values ranging from 15° to 70° are shown in Figure 1e. It reveals that the diffraction peaks of A1 can be indexed as those of the monoclinic phase of $SmPO_4$ crystal (JCPDS card no.: 01-084-0918). For example, the peaks at 27.537°, 29.420°, 31.796°, and 35.012°, respectively, correspond to the (2,0,0), (1,2,0), ($\bar{1}$,1,2), and ($\bar{2}$,0,2) planes of $SmPO_4$. And this is also consistent with the diffraction peaks of core−shell NPs. Besides, only amorphous silica powder was observed in the outer shell. Note that no single Eu^{3+} phases exist due to the initial small loading amount of Eu^{3+} ions and the fact that both Sm^{3+} and Eu^{3+} have very close atomic and electronic structures. Similar phenomena were observed by Wang and Wu.[26−28] To further confirm the existence of Eu^{3+} ions in the core−shell NPs, the EDS spectra were measured as shown in Figure 1f and Figure S1, indicating the existence of europium, oxygen, and silicon elements in the shell and samarium, oxygen, and phosphor elements in the $SmPO_4$ core. In summary, a core−shell nanostructure of samarium phosphates encapsulated into Eu^{3+}-doped silica shell has been successfully fabricated.

Since Eu^{3+} ions have an important role in the performance of solar cells, it is thus vital to determin the optimum doping amounts in the shell. However, because there is loss of Eu^{3+} during the preparation process, accurately controling the contents of the final percentage of Eu^{3+} within the silica shell is thus somewhat experimentally challenging. Next, the initial loading of Eu^{3+} was altered to study the effect of Eu^{3+} doping amounts on the performance of the solar cells whereas the loading amounts of Sm and Si were kept unchanged. Thus, different initial loading of Eu^{3+} was used and the IPCE measurements were performed to investigate the effect of the contents of Eu^{3+} on the device performances. As observed from Figure 2, a notable increase of IPCE around 400 nm can be observed when the contents of Eu^{3+} increases from 1 to 3 wt %, which originates from the enhancement of ET process between Sm^{3+} and Eu^{3+}, which will be discussed in detail later. Meanwhile, the broad IPCE curves covering the spectrum from 450 to 600 nm are almost independent of the contents of Eu^{3+}, exhibiting a maximum IPCE value of about 53%, and this is consistent with the UV−vis spectrum of P3HT as shown in Figure S2. The ET process converts the solar spectrum near 400 nm to 500−600 nm visible range that can be absorbed better by P3HT, thus leading to a notable increase in IPCE around 400 nm. However, to our surprise, with further adding of Eu^{3+} up to 5 wt %, the IPCE decreases. This decrease may be ascribed to the quenching of the luminescence that arises from

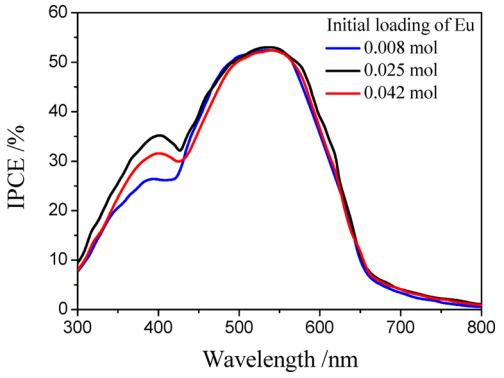

Figure 2. IPCE of core−shell NPs:TiO_2 BHJ solar cells with different initial loading amounts of Eu^{3+} in the silica shell under illumination of 400 nm laser.

the introducing of deleterious cross-relaxation by elevated doping levels.[21] Therefore, when the initial loading of Eu^{3+} is about 0.025 mol, the device exhibits the best performance.

It is known that the ideal solar cell materials should bear good optical absorption characteristics first. In order to reveal the ET process of lanthanide ions codoped core−shell NPs, the DC photoluminescence (PL) were carried out and shown in Figure 3. Figure 3a shows the schematic illustration of ET process in core−shell NPs. In the core−shell NPs, $SmPO_4$ core acts as a light-harvesting engine to absorb ultraviolet excitation light and subsequently transfers energy to the Eu^{3+} doped shell. Figure 3b shows the PL excitation and DC emission spectra of Eu^{3+} in the core−shell NPs. The PL excitation spectrum of core−shell NPs (Figure 3b, left) was dominated by the near-UV light excitation lines centered at ∼402 nm that correspond to the typical $^6H_{5/2} \rightarrow {}^4L_{15/2}$ transitions of Sm^{3+}.[38] The PL spectra of core−shell NPs were excited at 402 nm, followed by the emission of Eu^{3+} in the visible light range (Figure 3b right): the Eu^{3+} emission can be achieved via an ET process from the host (Sm^{3+}) to emitter (Eu^{3+}), resulting in the emission spectrum of core−shell NPs that consists of line peaks mainly locating at 592, 612, 650, and 701 nm, corresponding to the transitions of Eu^{3+} ions, i.e., $^5D_0 \rightarrow {}^7F_J$ (J = 1, 2, 3, 4).[39] In addition, the peaks at 527, 539, 618, 696 nm stem from the transitions of Eu^{3+} ions: $^5D_1 \rightarrow {}^7F_0$, $^5D_1 \rightarrow {}^7F_1$, $^5D_1 \rightarrow {}^7F_4$, and $^5D_1 \rightarrow {}^7F_5$, respectively.[14] Note that these luminescence bands are located in the absorption range of the P3HT (SI, Figure S2). Combining the excitation and emission spectra, the ultraviolet irradiation can be absorbed by the donor material in the HSCs via DC luminescence, which widens the light absorption range of the HSCs. Core−shell nanophosphors enable to fully utilize the down-conversion of ultraviolet absorption by Sm^{3+} in conjunction with the ET process without sacrificing the DC luminescence of Eu^{3+}. This unique core−shell nanophosphors architecture can allow full utilization of down-converted light and hold great promise in enhancing photovoltaic performance of solar cells.

3.2. Electron/Hole-Transport Dynamics of BHJs by Introducing the Core−Shell NPs. Apart from the good optical absorption characteristics, an ideal solar cell material also should have efficient charge-transport properties. To reveal the electron transport properties at the interface of acceptor/donor BHJs, the steady state and transient PL spectra were measured in Figure 4. Figure 4a shows the steady state PL results of donor (P3HT) neat film, core−shell NPs:TiO_2/P3HT BHJ film, respectively, following excitation at 500 nm.

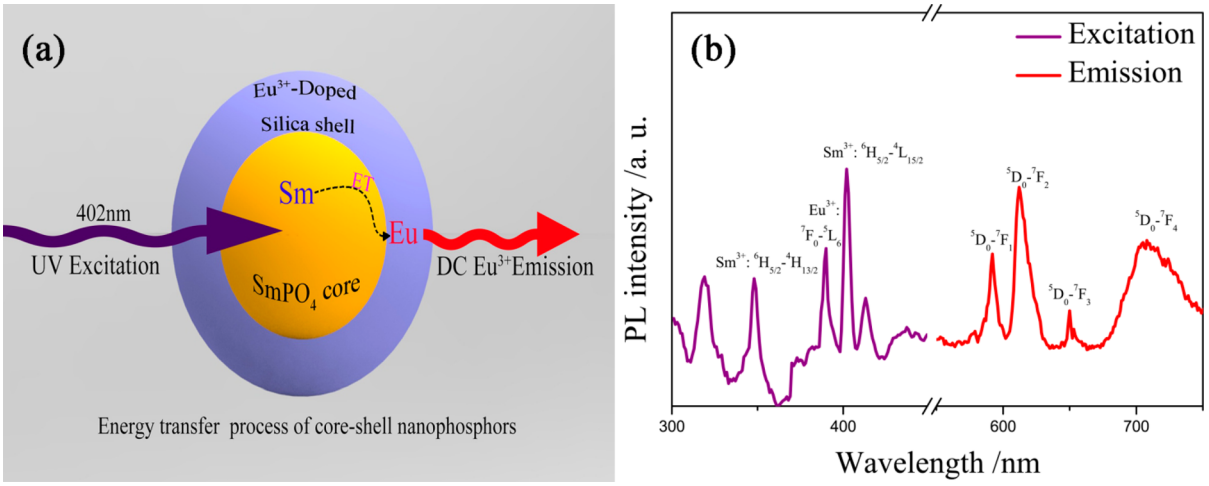

Figure 3. (a) Schematic design of a lanthanide-doped core−shell NPs for ET process. (b) PL excitation (λ_{em} = 614 nm) and DC emission (λ_{ex} = 402 nm) spectra for single crystalline $SmPO_4$@ Eu^{3+}-doped silica core−shell NPs.

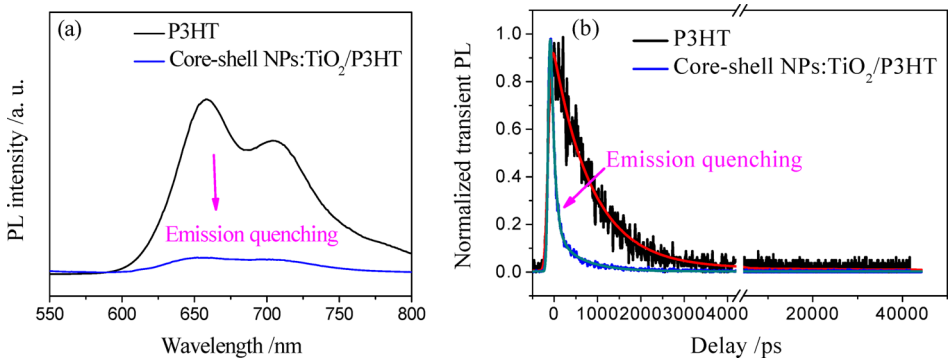

Figure 4. Steady state (a) and transient PL (b) for P3HT and core−shell NPs:TiO_2/P3HT films, respectively.

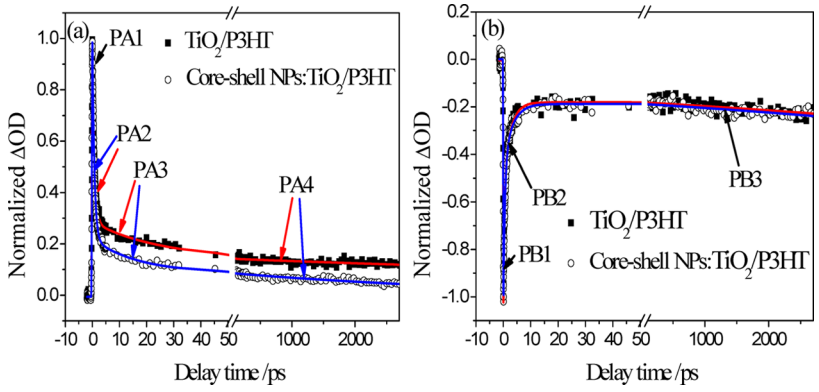

Figure 5. Normalized femtosecond transient absorption decays of core−shell NPs:TiO_2/P3HT (open circle) and TiO_2/P3HT (square) films excited at 400 nm (17 μJ cm^{-2}) probed at 650 nm (a) and at 602 nm (b), respectively. Solid lines are fitting curves with exponential components.

The emission of core−shell NPs:TiO_2/P3HT BHJ was quenched by over 90% than P3HT emission, because lots of the charges transport from donor to acceptor in BHJs.[6] However, the PL for the BHJ has not yet been completely quenched, which may be ascribed to the large pores of acceptor films and hence a greater volume of P3HT is not in direct contact with the core−shell NPs:TiO_2 acceptor. To further confirm the charge transport of BHJ, the transient PL spectroscopy was employed to characterize the samples. Figure 4b shows the transient PL signals for the P3HT neat film and core−shell NPs:TiO_2/P3HT BHJ, respectively. Under identical experimental conditions, the fast component of the PL signal of the P3HT was greatly reduced when the P3HT was interfaced with the electron extracting layer (core−shell NPs:TiO_2 acceptor). The high degrees of PL quenching indicates that strong charge transport exists in the blended donor/acceptor BHJ system. However, due to the limited temporal resoultion of ~60 ps, our time-resolved PL decay transients cannot accurately probe the doping effect (i.e., the tailoring of energy level of TiO_2 here) on electron transport because the electron transport lifetime is on the order of picoseconds.[40] What's more, because of the relatively poor singal to noise ratio (SNR),

Table 1. Lifetimes and the Amplitudes from Fits to TAS Decays Using the Linear Superposition of Electronic Contributions

	lifetime (τ) (amplitude)				
core−shell	τ_{vibl}/ps (A)	$\tau_{hot\text{-}e}$/ps (B)	τ_{re}/ns (C)	τ_{vibl2}/ps (A)	τ_h/ns (B)
NPs:TiO_2/P3HT	0.71 ± 0.01 (0.96)	16.7 ± 0.7 (0.16)	4.4 ± 0.2 (0.09)	0.75 ± 0.04 (−0.82)	6.9 ± 0.9 (−0.18)
TiO_2/P3HT	0.75 ± 0.01 (0.95)	30.2 ± 1.0 (0.15)	14.0 ± 1.5 (0.14)	0.80 ± 0.04 (−0.81)	6.9 ± 1.0 (−0.19)

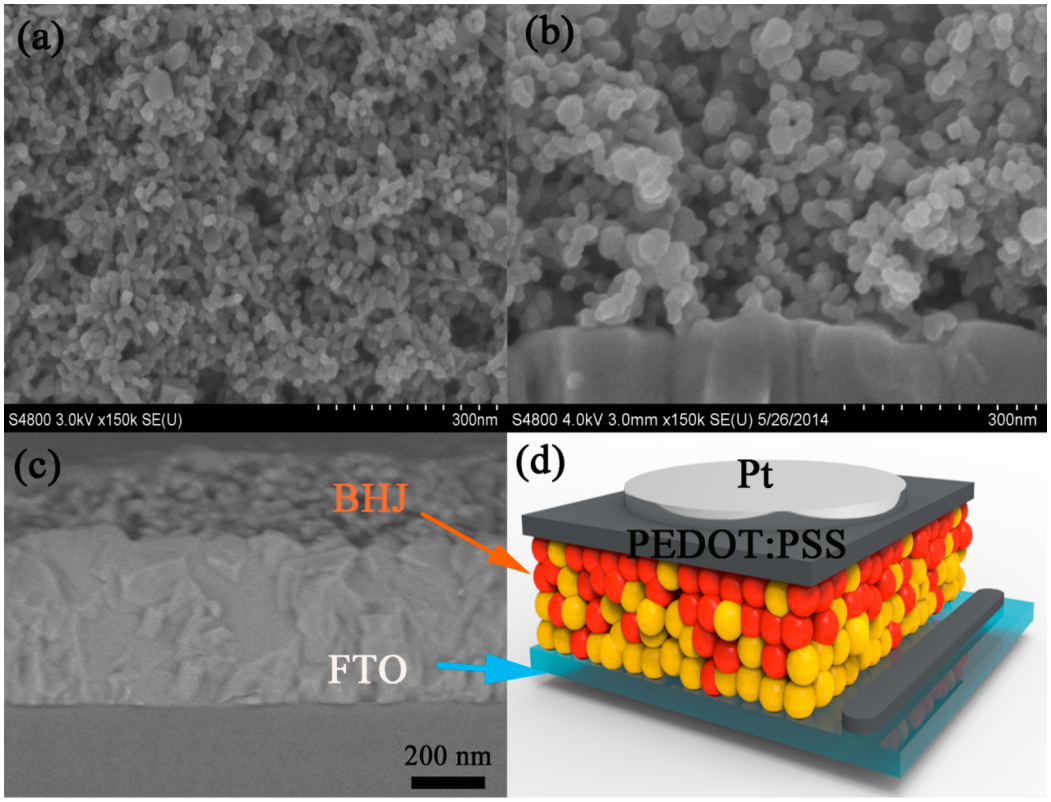

Figure 6. High resolution SEM image (a) and cross-sectional SEM image of core−shell NPs:TiO_2 (b), cross-sectional SEM image of BHJ device (c), and schematic diagram of the inorganic/organic HSCs (d).

it cannot effectively monitor all the photoexcited carriers. Therefore, femotosecond transient absorption spectroscopy with a temporal resolution of ∼120 fs and a high signal to noise ration (SNR; 10^{-4}) will be applied, and we would successfully acquire the electron transport time of BHJ system with or without incorporating the core−shell NPs.

The decay lifetime is an important parameter related to the charge-transport properties of material performance,[41] which can be studied by femotosecond transient absorption spectroscopy (TAS).[42−44] Figure S3 in the SI shows the TAS spectra of BHJs based on pure TiO_2/P3HT and blended core−shell NPs:TiO_2/P3HT, respectively. The positive band around 650 nm represents photoinduced excited state absorptions (PA), originating from the so-called sate-filling effects.[45] The negative band around 602 nm was ascribed to the photobleaching (PB) of the ground state absorption, which is consistent with the ultraviolet−visible absorption of P3HT (SI, Figure S2). Analysis of the PA and PB transients would provide detailed insight into the photoexcited electron and hole dynamics, respectively (Figure 5). We have decomposed the PA signals of these films into four dynamically distinct components that appear common to the inorganic/organic blend films. These components include: PA1, a scalar multiple of the laser pulse autocorrelation function that responses instantaneously to the applied laser field; PA2, nonradiative decay of hot electron in P3HT after the high photoenergy excitation (3.10 eV) with a vibronic relaxation time of τ_{vib1}; PA3, the hot electron transfer from donor to acceptor with transfer time of $\tau_{hot\text{-}e}$; PA4, the contribution of the recombination of the hot electron−hole pairs with a time constant τ_{re}. The PB transients are decomposed into three components: PB1, a scalar multiple of the laser pulse autocorrelation function; PB2, nonradiative decay of hot hole in P3HT a vibronic relaxation time of τ_{vib2}; PB3, the combined contribution of hole transfer from acceptor to donor with hole transfer time of τ_h and the geminate recombination of the electron−hole pairs. All these transients were fitted with exponential functions,[46] and the constants were sumarized in Table 1. We found that core−shell NPs have little influence on the hole transport from acceptor to donor, with almost the same transfer time τ_h = 6.9 ns. But with blended core−shell NPs:TiO_2 as the acceptor layer present, the hot electron transfer lifetime was shortened from 30.2 to 16.7 ps, i.e., more than 44% faster than the pure TiO_2 acceptor. Highly efficient hot electron transport represents one of the most promising technologies for applications in photovoltaic devices. Absorption of high-energy photons results in "hot" electrons and holes, which are both electronically excited and thermally activated and will lose most of their energies by emitting phonons (hot carrier cooling) without contributing to electric power.[43,47] Efficient HSCs would not only absorb a wide range

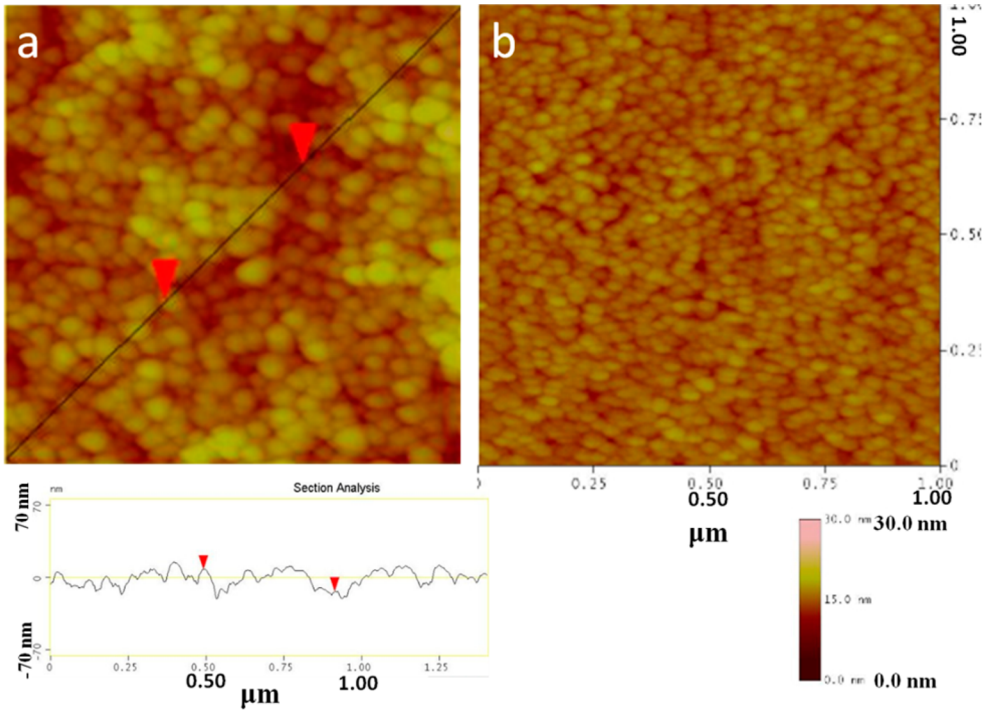

Figure 7. AFM images of the TiO_2 acceptor with height profile (a) and with flattening processing (b). Below part a is the height profile along the line and the height difference between the two marked arrows is about 20 nm; the color gradient in the datascale at the right bottom corner indicates the profile of height distribution in part b.

of photon energies but also extract a large fraction of the energy to give high efficiencies by extracting "hot" carriers before they thermalize to the band edges. After doping with core−shell NPs, the hot electron transfer becomes more competitive and core−shell architecture may provide special channel that benifits hot electron transfer. Thus, the core−shell NPs can play an important role in the BHJ device performance. The enhanced charge transports from donor to acceptor that can improve photovoltaci performances of solar cells are mainly ascribed to the energy level alignment of acceptor induced by the core−shell nanophosphors. The conduction band (CB) of TiO_2 have been elevated by 0.38 eV, the energy offest between CB of TiO_2 and the lowest unoccupied molecular orbital of P3HT has been narrowed (SI, Figure S4 and Table S1), thus leading to the enhanced electron transfer at the interface. But, the valence band (VB) of TiO_2 stays almost constant, and thereby, the hole tranfer lifetime virtually does not change.

3.3. Photovoltaic Characterization of the HSCs. To reveal the efficient electron-transport of BHJ by incorporating the core−shell NPs, HSCs based on the two different BHJ with or without incorporating the core−shell NPs were assembled for comparison. The morphology of acceptor layer is shown in Figure 6a and b, and it can be observed that although the contents of core−shell NPs are low, nonetheless a certain number of larger grains (~50 nm) still can be observed and have been dispersed into nanocrystal TiO_2 (particle size of ~20 nm). The surface of the acceptor layer clearly exhibits a loose structure,[48] which on one hand favors the improvement of p−n contact for BHJ and provides channels for P3HT solution across the acceptor layer; on the other hand, this kind of structure is prone to readily adsorb P3HT molecules by trapping the P3HT solution in the porosity.[36] The cross-sectional SEM image of the BHJ and the schematic diagram of the HSC are shown in Figure 6c and d, respectively. This reveals that the different layers and their individual thickness of FTO, core−shell NPs:TiO_2, and P3HT can be clearly distinguished. Especially, the thickness of BHJ including core−shell NPs:TiO_2 and P3HT was estimated to be about 250 nm. The intimatly contacting interface and suitable thickness of BHJ mode make for p−n contact and electron transport (from donor to acceptor).[49]

Moreover, the morphology of the core−shell NPs doped TiO_2 acceptor film was further characterized by AFM as shown in Figure 7. As estimated from Figure 7a, the topographic height was estimated to be 20 nm with a surface roughness of about 10 nm according to our AFM statistical analysis and this is in reasonable agreement with the results obtained from Figure 7b, in which most of the heights are in the range of 20−25 nm.

The photovoltaic performances of HSCs based on the different BHJs with different amounts of core−shell NPs were examined (Figure 8), and photovoltaic parameters are summarized in Table 2. As observed from Figure 8, under the identical experimental conditions, it is evident that the HSCs made from core−shell NPs:TiO_2 BHJ demonstrate better photovoltaic performances than pure TiO_2/P3HT BHJ. With the increase of the doping amounts of nanophosphors, both open-circuit voltage V_{oc} (from 0.670 to 0.727 V) and short-circuit current density J_{sc} (from 5.91 to 7.97 mA cm^{-2}) increase gradually while the filling factor (FF) only increases slightly, thus leading to a gradual enhancement of PCE from 1.98% for pure TiO_2 to a maximum PCE of 3.3% at 5 wt %. Note that this efficiency is higher than those of most of the other inroganic/organic hybrid solar cells so far.[6−8] This demonstrates that the core−shell NP indeed is critical to enhance electron-transport properties of BHJs and the photovoltaic performance of HSCs. Besides, it is worth mentioning that the doping amount of core−shell nano-

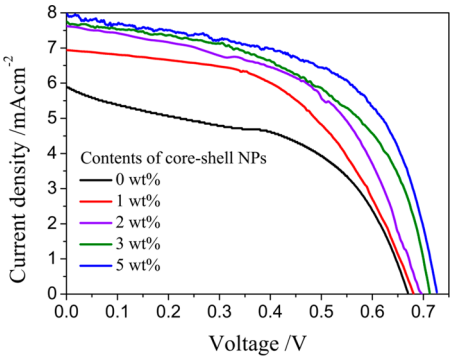

Figure 8. J–V characteristics curves of HSCs from TiO_2/P3HT BHJ (black) and core–shell NPs:TiO_2/P3HT BHJ with different amounts of dopants.

Table 2. Photovoltaic Parameters of the HSCs Based on Different BHJs

contents of core–shell NPs [wt %]	V_{oc} [V]	J_{sc} [mA cm^{-2}]	FF	η^a [%]
0%	0.670	5.91	0.50	1.98
1%	0.679	6.95	0.54	2.55
2%	0.697	7.60	0.55	2.91
3%	0.713	7.75	0.55	3.04
5%	0.727	7.97	0.57	3.30

$^a\eta = J_{sc}V_{oc}FF/P_{in}$, where P_{in} = 100 mW cm^{-2} (AM 1.5).

phosphors is 5.0 wt % at most relative to (core–shell NPs:TiO_2) acceptor film throughout the whole text except when otherwise indicated. This is because when exceeding 5.0 wt %, it is not ready to form a flat acceptor film. Last but not least, this work is initially motivated by understanding the underlying photogeneration dynamics of core–shell NPs in HSCs, which should provide some insight into the designing rule for optimizing photovoltaic devices in future.

4. CONCLUSIONS

In summary, we have successfully prepared photoluminescent nanophosphor $SmPO_4$@Eu^{3+}-doped SiO_2 composite, namely the encapsulation of $SmPO_4$ nanoparticles into Eu^{3+}-doped SiO_2 shell. The energy transfer of the resulting core–shell structures from Sm^{3+} to emitters Eu^{3+} was studied by PL measurements, in which the potential to tune DC properties by combining energy migration and core–shell nanostructure has been demonstrated. To reveal the doping effect of core–shell NPs on electron-transport properties, BHJ solar cells with the intimate interface and suitable thickness of a BHJ were prepared with or without incorporating core–shell NPs for comparison. The underlying electron-transport dynamics of BHJs by incorporating core–shell NPs were clearly unveiled by steady state, transient PL, and femtosecond transient absorption spectroscopies. The high degrees of PL quenching indicate that strong charge transport exists in the blended core–shell NPs:TiO_2/P3HT BHJ devices. Although the hole transport almost remains unchanged, the electron transport lifetime was shortened from 30.2 to 16.7 ps. The photovoltaic performances of core–shell NPs-based BHJ solar cells can be substantially improved in both V_{oc} and J_{sc}, thus leading to an improved PCE from 1.98% to 3.30%. Such enhancements are mainly ascribed to the excellent DC photoluminescent properties, efficient electron-transport, and energy transfer in HSCs which benefited from the unique core–shell architectures and energy level alignment. The core–shell NPs, as multiplexed luminescent nanobiolabels and photocatalytic materials, may have versatile and promising applications. The research described here provides a general approach to constructing a new class of luminescent materials with unique core–shell architecture, which achieves synergistic properties thanks to the structural distinctiveness and property diversity and potentially enables the tailoring of energy bands within a nanoscopic region in future work.

■ ASSOCIATED CONTENT

Supporting Information

In-depth characterization of the BHJs used in this study. Briefly, Figure S1 contains EDS spectra and TEM images of the $SmPO_4$ core and the Eu^{3+}-doped silica shell, respectively. Figure S2 showed the ultraviolet–visible absorption of P3HT methylbenzene solution. Figures S3 and S4 show the transient absorption spectrum decay and CV characteristics of the core–shell NPs:TiO_2/P3HT film, respectively. Table S1 shows the electrochemical parameters obtained from CV curves. This material is available free of charge via the Internet at http://pubs.acs.org.

■ AUTHOR INFORMATION

Corresponding Authors

*Tel./Fax: +86 791 86453203. E-mail: qhli@hqu.edu.cn.
*E-mail: weifu.sun518@gmail.com.

Notes

The authors declare no competing financial interest.

■ ACKNOWLEDGMENTS

The authors gratefully acknowledge the financial support of the Natural Science Foundation of China (61366003), the science and technology project of the Education Department of Jiangxi Province, China (GJJ12449, GJJ14533), and Aviation Science Fund of China (2013ZF56025).

■ REFERENCES

(1) Zhao, L.; Lin, Z. Crafting Semiconductor Organic–Inorganic Nanocomposites via Placing Conjugated Polymers in Intimate Contact with Nanocrystals for Hybrid Solar Cells. *Adv. Mater.* **2012**, *24*, 4353–4368.
(2) Chen, Z.; Zhang, H.; Yu, W.; Li, Z.; Hou, J.; Wei, H.; Yang, B. Inverted Hybrid Solar Cells from Aqueous Materials with a PCE of 3.61%. *Adv. Energy Mater.* **2013**, *3*, 433–437.
(3) Gur, I.; Fromer, N. A.; Chen, C.-P.; Kanaras, A. G.; Alivisatos, A. P. Hybrid Solar Cells with Prescribed Nanoscale Morphologies Based on Hyperbranched Semiconductor Nanocrystals. *Nano Lett.* **2006**, *7*, 409–414.
(4) Sung, Y.-H.; Liao, W.-P.; Chen, D.-W.; Wu, C.-T.; Chang, G.-J.; Wu, J.-J. Room-Temperature Tailoring of Vertical ZnO Nanoarchitecture Morphology for Efficient Hybrid Polymer Solar Cells. *Adv. Funct. Mater.* **2012**, *22*, 3808–3814.
(5) Lee, J.; Mubeen, S.; Hernandez-Sosa, G.; Sun, Y.; Toma, F. M.; Stucky, G. D.; Moskovits, M. High-Efficiency Panchromatic Hybrid Schottky Solar Cells. *Adv. Mater.* **2013**, *25*, 256–260.
(6) Shoaee, S.; Briscoe, J.; Durrant, J. R.; Dunn, S. Acoustic Enhancement of Polymer/ZnO Nanorod Photovoltaic Device Performance. *Adv. Mater.* **2014**, *26*, 263–268.
(7) Wang, X.; Ishwara, T.; Gong, W.; Campoy-Quiles, M.; Nelson, J.; Bradley, D. D. C. High-Performance Metal-Free Solar Cells Using Stamp Transfer Printed Vapor Phase Polymerized Poly(3,4-Ethylenedioxythiophene) Top Anodes. *Adv. Funct. Mater.* **2012**, *22*, 1454–1460.

(8) Huang, C.-Y.; Wang, D.-Y.; Wang, C.-H.; Chen, Y.-T.; Wang, Y.-T.; Jiang, Y.-T.; Yang, Y.-J.; Chen, C.-C.; Chen, Y.-F. Efficient Light Harvesting by Photon Downconversion and Light Trapping in Hybrid ZnS Nanoparticles/Si Nanotips Solar Cells. *ACS Nano* **2010**, *4*, 5849−5854.
(9) Maraghechi, P.; Labelle, A. J.; Kirmani, A. R.; Lan, X.; Adachi, M. M.; Thon, S. M.; Hoogland, S.; Lee, A.; Ning, Z.; Fischer, A.; Amassian, A.; Sargent, E. H. The Donor−Supply Electrode Enhances Performance in Colloidal Quantum Dot Solar Cells. *ACS Nano* **2013**, *7*, 6111−6116.
(10) Gao, F.; Ren, S.; Wang, J. The Renaissance of Hybrid Solar Cells: Progresses, Challenges, and Perspectives. *Energy Environ. Sci.* **2013**, *6*, 2020−2040.
(11) Wu, J.; Li, Y.; Tang, Q.; Yue, G.; Lin, J.; Huang, M.; Meng, L. Bifacial Dye-Sensitized Solar Cells: A Strategy to Enhance Overall Efficiency Based on Transparent Polyaniline Electrode. *Sci. Rep.* **2014**, *4*, 4028.
(12) He, B.; Tang, Q.; Wang, M.; Ma, C.; Yuan, S. Complexation of Polyaniline and Graphene for Efficient Counter Electrodes in Dye-Sensitized Solar Cells: Enhanced Charge Transfer Ability. *J. Power Sources* **2014**, *256*, 8−13.
(13) Xie, Y.; Huang, N.; You, S.; Liu, Y.; Sebo, B.; Liang, L.; Fang, X.; Liu, W.; Guo, S.; Zhao, X.-Z. Improved Performance of Dye-Sensitized Solar Cells by Trace Amount Cr-Doped TiO_2 Photoelectrodes. *J. Power Sources* **2013**, *224*, 168−173.
(14) Massihi, N.; Mohammadi, M. R.; Bakhshayesh, A. M.; Abdi-Jalebi, M. Controlling Electron Injection and Electron Transport of Dye-Sensitized Solar Cells Aided by Incorporating CNTs into a Cr-Doped TiO_2 Photoanode. *Electrochim. Acta* **2013**, *111*, 921−929.
(15) Melhem, H.; Simon, P.; Wang, J.; Di Bin, C.; Ratier, B.; Leconte, Y.; Herlin-Boime, N.; Makowska-Janusik, M.; Kassiba, A.; Bouclé, J. Direct Photocurrent Generation from Nitrogen Doped TiO_2 Electrodes in Solid-State Dye-Sensitized Solar Cells: Towards Optically-Active Metal Oxides for Photovoltaic Applications. *Sol. Energy Mater. Sol. Cells* **2013**, *117*, 624−631.
(16) Kim, Y. S.; Yu, B.-K.; Kim, D.-Y.; Kim, W. B. A Hybridized Electron-Selective Layer Using Sb-Doped SnO_2 Nanowires for Efficient Inverted Polymer Solar Cells. *Sol. Energy Mater. Sol. Cells* **2011**, *95*, 2874−2879.
(17) Scharber, M. C.; Mühlbacher, D.; Koppe, M.; Denk, P.; Waldauf, C.; Heeger, A. J.; Brabec, C. J. Design Rules for Donors in Bulk-Heterojunction Solar Cells—Towards 10% Energy-Conversion Efficiency. *Adv. Mater.* **2006**, *18*, 789−794.
(18) Brédas, J.-L.; Cornil, J.; Heeger, A. J. The Exciton Binding Energy in Luminescent Conjugated Polymers. *Adv. Mater.* **1996**, *8*, 447−452.
(19) Muntwiler, M.; Yang, Q.; Tisdale, W. A.; Zhu, X. Y. Coulomb Barrier for Charge Separation at an Organic Semiconductor Interface. *Phys. Rev. Lett.* **2008**, *101*, 196403.
(20) Treu, J.; Bormann, M.; Schmeiduch, H.; Döblinger, M.; Morkötter, S.; Matich, S.; Wiecha, P.; Saller, K.; Mayer, B.; Bichler, M.; Amann, M.-C.; Finley, J. J.; Abstreiter, G.; Koblmüller, G. Enhanced Luminescence Properties of InAs−InAsP Core−Shell Nanowires. *Nano Lett.* **2013**, *13*, 6070−6077.
(21) Wang, F.; Deng, R.; Wang, J.; Wang, Q.; Han, Y.; Zhu, H.; Chen, X.; Liu, X.; Tuning Upconversion, Through Energy Migration in Core−Shell Nanoparticles. *Nat. Mater.* **2011**, *10*, 968−973.
(22) Wong, H.-T.; Chan, H. L. W.; Hao, J. H. Magnetic and Luminescent Properties of Multifunctional GdF_3:Eu^{3+} Nanoparticles. *Appl. Phys. Lett.* **2009**, *95*, 022512.
(23) Hou, Z.; Yang, P.; Li, C.; Wang, L.; Lian, H.; Quan, Z.; Lin, J. Preparation and Luminescence Properties of YVO_4:Ln and Y(V, P)O_4:Ln (Ln = Eu^{3+}, Sm^{3+}, Dy^{3+}) Nanofibers and Microbelts by Sol−Gel/Electrospinning Process. *Chem. Mater.* **2008**, *20*, 6686−6696.
(24) Abdul Jalil, R.; Zhang, Y. Biocompatibility of Silica Coated $NaYF_4$ Upconversion Fluorescent Nanocrystals. *Biomaterials* **2008**, *29*, 4122−4128.
(25) Selinsky, R. S.; Ding, Q.; Faber, M. S.; Wright, J. C.; Jin, S. Quantum Dot Nanoscale Heterostructures for Solar Energy Conversion. *Chem. Soc. Rev.* **2013**, *42*, 2963−2985.
(26) Wu, J.; Wang, J.; Lin, J.; Xiao, Y.; Yue, G.; Huang, M.; Lan, Z.; Huang, Y.; Fan, L.; Yin, S.; Sato, T. Dual Functions of YF_3:Eu^{3+} for Improving Photovoltaic Performance of Dye-Sensitized Solar Cells. *Sci. Rep.* **2013**, *3*, 2058.
(27) Wu, J.; Wang, J.; Lin, J.; Lan, Z.; Tang, Q.; Huang, M.; Huang, Y.; Fan, L.; Li, Q.; Tang, Z. Enhancement of the Photovoltaic Performance of Dye-Sensitized Solar Cells by Doping $Y_{0.78}Yb_{0.20}Er_{0.02}F_3$ in the Photoanode. *Adv. Energy Mater.* **2012**, *2*, 78−81.
(28) Wang, J.; Wu, J.; Lin, J.; Huang, M.; Huang, Y.; Lan, Z.; Xiao, Y.; Yue, G.; Yin, S.; Sato, T. Application of Y_2O_3:Er^{3+} Nanorods in Dye-Sensitized Solar Cells. *ChemSusChem* **2012**, *5*, 1307−1312.
(29) Liu, Y.; Tu, D.; Zhu, H.; Li, R.; Luo, W.; Chen, X. A Strategy to Achieve Efficient Dual-Mode Luminescence of Eu^{3+} in Lanthanides Doped Multifunctional $NaGdF_4$ Nanocrystals. *Adv. Mater.* **2010**, *22*, 3266−3271.
(30) Zhang, T.; Ge, J.; Hu, Y.; Yin, Y. A General Approach for Transferring Hydrophobic Nanocrystals into Water. *Nano Lett.* **2007**, *7*, 3203−3207.
(31) Park, J.-U.; Lee, H. J.; Cho, W.; Jo, C.; Oh, M. Facile Synthetic Route for Thickness and Composition Tunable Hollow Metal Oxide Spheres from Silica-Templated Coordination Polymers. *Adv. Mater.* **2011**, *23*, 3161−3164.
(32) Stöber, W.; Fink, A.; Bohn, E. Controlled Growth of Monodisperse Silica Spheres in the Micron Size Range. *J. Colloid Interface Sci.* **1968**, *26*, 62−69.
(33) Liu, H.; Wang, T.; Zhang, L.; Li, L.; Wang, Y. A.; Wang, C.; Su, Z. Selected-Control Fabrication of Multifunctional Fluorescent−Magnetic Core−Shell and Yolk−Shell Hybrid Nanostructures. *Chem.—Eur. J.* **2012**, *18*, 3745−3752.
(34) Lee, H. J.; Park, J.-U.; Choi, S.; Son, J.; Oh, M. Synthesis and Photoluminescence Properties of Eu^{3+}-Doped Silica@Coordination Polymer Core−Shell Structures and Their Calcinated Silica@Gd_2O_3:Eu and Hollow Gd_2O_3:Eu Microsphere Products. *Small* **2013**, *9*, 561−569.
(35) Wu, J.; Hao, S.; Lin, J.; Huang, M.; Huang, Y.; Lan, Z.; Li, P. Crystal Morphology of Anatase Titania Nanocrystals Used in Dye-Sensitized Solar Cells. *Cryst. Growth Des.* **2007**, *8*, 247−252.
(36) Li, Q.; Wu, J.; Tang, Q.; Lan, Z.; Li, P.; Lin, J.; Fan, L. Application of Microporous Polyaniline Counter Electrode for Dye-Sensitized Solar Cells. *Electrochem. Commun.* **2008**, *10*, 1299−1302.
(37) Wu, J. H.; Hao, S.; Lan, Z.; Lin, J. M.; Huang, M. L.; Huang, Y. F.; Li, P. J.; Yin, S.; Satot, T. An All-Solid-State Dye-Sensitized Solar Cell-Based Poly(N-alkyl-4-vinyl-pyridine iodide) Electrolyte with Efficiency of 5.64%. *J. Am. Chem. Soc.* **2008**, *130*, 11568−11569.
(38) Li, G.; Hou, Z.; Peng, C.; Wang, W.; Cheng, Z.; Li, C.; Lian, H.; Lin, J. Electrospinning Derived One-Dimensional LaOCl: Ln^{3+} (Ln = Eu/Sm, Tb, Tm) Nanofibers, Nanotubes and Microbelts with Multicolor-Tunable Emission Properties. *Adv. Funct. Mater.* **2010**, *20*, 3446−3456.
(39) Dejneka, M. J.; Streltsov, A.; Pal, S.; Frutos, A. G.; Powell, C. L.; Yost, K.; Yuen, P. K.; Muller, U.; Lahiri, J. Rare Earth-Doped Glass Microbarcodes. *Proc. Natl. Acad. Sci. U.S.A.* **2003**, *100*, 389−393.
(40) Ohkita, H.; Ito, S. Transient Absorption Spectroscopy of Polymer-Based Thin-Film Solar Cells. *Polymer* **2011**, *52*, 4397−4417.
(41) He, B.; Tang, Q.; Luo, J.; Li, Q.; Chen, X.; Cai, H. Rapid Charge-Transfer in Polypyrrole−Single Wall Carbon Nanotube Complex Counter Electrodes: Improved Photovoltaic Performances of Dye-Sensitized Solar Cells. *J. Power Sources* **2014**, *256*, 170−177.
(42) Clarke, T. M.; Durrant, J. R. Charge Photogeneration in Organic Solar Cells. *Chem. Rev.* **2010**, *110*, 6736−6767.
(43) Tisdale, W. A.; Williams, K. J.; Timp, B. A.; Norris, D. J.; Aydil, E. S.; Zhu, X. Y.; Hot-Electron Transfer, From Semiconductor Nanocrystals. *Science* **2010**, *328*, 1543−1547.
(44) Guo, J.; Ohkita, H.; Benten, H.; Ito, S. Charge Generation and Recombination Dynamics in Poly(3-hexylthiophene)/Fullerene Blend

Films with Different Regioregularities and Morphologies. *J. Am. Chem. Soc.* **2010**, *132*, 6154−6164.
(45) Bakulin, A. A.; Hummelen, J. C.; Pshenichnikov, M. S.; van Loosdrecht, P. H. M. Ultrafast Hole-Transfer Dynamics in Polymer/PCBM Bulk Heterojunctions. *Adv. Funct. Mater.* **2010**, *20*, 1653−1660.
(46) McMorrow, D.; Lotshaw, W. T.; Kenney-Wallace, G. A. Femtosecond optical Kerr studies on the Origin of the Nonlinear Responses in Simple Liquids. *IEEE J. Quantum Elect.* **1988**, *24*, 443−454.
(47) Kamat, P. V. Photovoltaics: Capturing Hot Electrons. *Nat. Chem.* **2010**, *2*, 809−810.
(48) He, B.; Meng, X.; Tang, Q. Low-Cost Counter Electrodes From CoPt Alloys For Efficient Dye-Sensitized Solar Cells. *ACS Appl. Mater. Interfaces* **2014**, *6*, 4812−4818.
(49) Shaw, P. E.; Ruseckas, A.; Samuel, I. D. W. Exciton Diffusion Measurements in Poly(3-hexylthiophene). *Adv. Mater.* **2008**, *20*, 3516−3520.